Biometric Verification Using Thermal Images of Palm-Dorsa Vein Patterns

Chih-Lung Lin and Kuo-Chin Fan, *Member, IEEE*

***Abstract*—A novel approach to personal verification using the thermal images of palm-dorsa vein patterns is presented in this paper. The characteristics of the proposed method are that no prior knowledge about the objects is necessary and the parameters can be set automatically. In our work, an infrared (IR) camera is adopted as the input device to capture the thermal images of the palm-dorsa. In the proposed approach, two of the finger webs are automatically selected as the datum points to define the region of interest (ROI) on the thermal images. Within each ROI, feature points of the vein patterns (FPVPs) are extracted by modifying the basic tool of watershed transformation based on the properties of thermal images. According to the heat conduction law (the Fourier law), multiple features can be extracted from each FPVP for verification. Multiresolution representations of images with FPVPs are obtained using multiple multiresolution filters (MRFs) that extract the *dominant points* by filtering miscellaneous features for each FPVP. A hierarchical integrating function is then applied to integrate multiple features and multiresolution representations. The former is integrated by an inter-to-intra personal variation ratio and the latter is integrated by a positive Boolean function. We also introduce a logical and reasonable method to select a trained threshold for verification. Experiments were conducted using the thermal images of palm-dorsas and the results are satisfactory with an acceptable accuracy rate (FRR:2.3% and FAR:2.3%). The experimental results demonstrate that our proposed approach is valid and effective for vein-pattern verification.**

***Index Terms*—Inter-to-intra personal variation ratio, multiple multiresolution filters, positive Boolean function (PBF), vein-pattern verification, watershed transformation.**

I. Introduction

RECENTLY, personal verification has become an important and high-demand technique for security access systems. Traditional personal verification methods, such as passwords, personal identification numbers (PINs), magnetic swipe cards, keys, and smart cards offer only limited security and are unreliable. For example, cards or keys may be lost or stolen, and PINs may be known by unauthorized persons. Fortunately, human physiological features possess the properties, such as universality, uniqueness, permanence, collectability, acceptability, and circumvention [1]. In order to remedy security problems inherent in traditional personal verification methods, biometric verification techniques have been intensively studied and developed to improve the reliability of personal verification.

All biometric verification techniques deal with various human physiological features including fingerprints, hand geometry, handwritten signatures, retinal patterns, and facial images [1]. In addition, the use of infrared (IR) images of biological features, such as the IR images of faces [1], [2] and the subcutaneous vascular network of the palm-dorsum, has also been investigated [3], [4]. Factors that may influence the popularity, applicability and performance of biometric verification techniques are uniqueness, repeatability, maximum throughput, whether operable under controlled light or not, invasiveness or noninvasiveness, immunity from forgery, successful identification of dark-skinned subjects, false rejection rate (FRR) and false acceptance rate (FAR), ease of use, user cooperation, cleanliness and so on. Up to now, it is not surprising that there has been no biometric verification technique that can satisfy all these requirements [5].

In this paper, we will present a novel personal verification method based on the vein patterns of palm-dorsa. As we know, a vein pattern exists on the skin surface between the roots of the five fingers and the wrist of the palm-dorsum. This pattern offers stable, unique and repeatable features for personal identification purposes [1].

Many verification technologies utilizing the biometric features of the palm have been developed [6]–[14] over the past decade. Han *et al.* [6] applied Sobel and morphological operators to extract the palmprint feature points from palm images. Then, they used the template matching with normalized correlation function and the backpropagation neural network to verify the identity of persons. You *et al.* [7] applied the texture energy of palmprint for coarse-level identification. Feature points were then extracted for fine-level identification. Lin *et al.* [8] extracted a wide line integrated profile (WLIP), a variation of the wide line integrated profile (VWLIP), and finger width (FW) features from finger images. The similarities of the first two features and the dissimilarities between the third feature were measured using a correlation function and the Euclidean distance, respectively. Verification was accomplished by a fuzzy inference engine based on the similarity/dissimilarity measures. Han *et al.* [9] extracted the features of finger width, length, and the palmprint, put these features into a principal component analysis (PCA) process to filter meaningful features, and used the generalized learning vector quantization (GLVQ) approach to verify the identity of persons. Jain *et al.* [10] extracted hand shape features. A deformable matching technique was then applied to match the hand shapes, and a shape distance was defined to evaluate the hand shape similarities. Zhang *et al.* [11] transferred palmprints to line sections. They applied the datum point-invariant characteristics and the line-matching technique to verify palmprint features. Joshi *et al.* [12] utilized the medius finger creases to generate a finger crease profile and then trans-

Manuscript received October 29, 2002; revised June 5, 2003.

The authors are with the Institute of Computer Science and Information Engineering,, National Central University, Chung-Li, 32054, Taiwan, R.O.C. (e-mail: kcfan@csie.ncu.edu.tw; linclr@yahoo.com.tw).

Digital Object Identifier 10.1109/TCSVT.2003.821975

formed this profile to a WLIP. They adopted a normalized correlation function to determine the similarities of different persons. Im *et al.* [13], [14] employed a CCD camera to capture vein-pattern images. Their research focuses on implementing fixed-point operation to improve the verification speed and reduce the hardware cost. Rice [3] used IR LEDs and IR-sensitive photodiodes in an array as the sensor to capture the infrared images of palm-dorsa. The images were transferred to binary images and the vein patterns were exhibited. An exclusive OR operator was performed on two binary images and the output of the operator is used as a score to evaluate the similarity between the two images. Cross *et al.* [4] applied thermal images of the subcutaneous vascular network of the back of the hand for biometric identification. This technique needed an IR light source to provide sufficient IR light within the 0.7–1.4-μm spectrum for a CCD camera to capture the thermal images. Finally, they used constrained sequential correlation to match the vein signatures.

Generally speaking, high-quality images retain detailed information of biometric features. As a consequence, the information derived from biometric features will be richer, and the verification rate will be higher. Thus, the high-quality images of biometric features are a prerequisite for a high-verification-rate system. In order to capture high-quality images and maintain the characteristic details of biometric features, all such methods need sufficient light sources (include visible or infrared) for capturing the images. All methods are constrained by the lighting conditions. The pattern of blood vessels is hardwired into the body at birth and remains relatively unaffected by aging, except for predictable growth, which is also the case with fingerprints [1]. To overcome the drawbacks caused by inadequate lighting conditions and maintain the verification accuracy, we develop a reliable and robust system that relies on the vein patterns in thermal images of the palm-dorsa taken under all lighting conditions including total darkness.

The remainder of the paper is organized as follows. In Section II, we will briefly describe the characteristics of the equipment used in capturing the thermal images of the palm-dorsa. The collection and establishment of the palm-dorsa vein-pattern database is also addressed in the section. The methods used for preprocessing and locating the region of interest (ROI) of the palm-dorsa vein-pattern images are presented in Section III. Section IV discusses the procedures used in extracting the feature points of vein pattern (FPVP) and the extraction of multiple vein-pattern features from each FPVP. Multiresolution analysis (MRA) using multiresolution filters (MRFs) is addressed in Section V to extract the *dominant points* of each FPVP as the multiresolution representation. The integration functions of multiple features and multiresolution representation are discussed in Section VI to enhance the discrimination capability. Section VII presents the scheme of automatic selection of the training threshold for verification. Experimental results are demonstrated in Section VIII to verify the validity of the proposed approach. Finally, concluding remarks are given in Section IX.

Shown in Fig. 1 is the block diagram of the proposed approach. First, the thermal images of the palm-dorsa are captured by an IR camera as the input data. Then, a median filter is employed to process the thermal images to remove noise. The four finger-web locations are found and the square ROI is obtained based on the extracted second and fourth finger webs. Next, according to the characteristics of thermal images, FPVPs within each ROI are extracted by modifying the basic tool of watershed transformation. Multiple features can thereby be extracted from each FPVP based on the heat conduction law (the Fourier law) for verification. Moreover, multiresolution representations of images can also be obtained using multiple MRFs that extract the *dominant points* by filtering miscellaneous features for each FPVP. A hierarchical integrating function is then applied to integrate multiple features and multiresolution representations. The former is integrated by an inter-to-intra personal variation ratio (weights) and the latter is integrated by a positive Boolean function (PBF). A logical and reasonable method is introduced to select a trained threshold for verification. Generally speaking, there are two main stages in the proposed approach. One is the enrollment stage that constructs the template library. The other is the verification stage in which the identity of the test samples is verified.

II. Thermal Images Collection

To utilize vein patterns for verification, we must consider a very important issue, which is how to obtain the vein-pattern images. The vein pattern on the palm-dorsum is not easy to observe in visible light. Skin surface features [15], such as moles, warts, scars, pigmentation, and hair usually cover the vein pattern. In addition, subcutaneous fat and hand gesturing may also obscure the visibility of the vein pattern. Fortunately, the vein differs in temperature from the surrounding skin and the skin possesses a temperature gradient. Based on these two properties and the well-known heat radiation law, the Stefan–Boltzmann law, thermal images of the vein patterns can be generated as follows:

$$W = \varepsilon \cdot \sigma \cdot T^4 \tag{1}$$

where W is the radiant emittance $(\mathrm{W/cm^2})$, ε is the emissivity, σ is the Stefan–Boltzmann constant $(\cong 5.6705 \times 10^{-12}\ \mathrm{W/cm^2\ K^4})$, and T is the temperature (K) of the object surface. For human skin, ε is estimated to be 0.98 to 0.99 [16]. The greatest intensity of IR radiation emitted by the human body is about 10 $\mathrm{mW/cm^2}$ in the range of 3–14 μm [17], which is dependent on the emissivity of the skin, the skin temperature, the air molecules, the humidity of the air, and the distance between the IR camera and the object. The well-known Planck curve, shown in Fig. 2, illustrates the relationship between the spectrum radiant emittance and the wavelength [18]. The IR transmission spectra for the atmosphere are 3–5 and 8–14 μm, as shown in Fig. 3 [19], which means that the radiant emittance of the IR spectrum at 3–5 and 8–14 μm possesses only minimum attenuation in the atmosphere. By analyzing (1), σ is a constant and ε is also a constant for individuals. The IR detector is packaged in a Dewar flask at the back of the lens. It does not come directly into contact with the air, so the influence of convection can be ignored. The temperature T of the skin surface is the only variable which dominates the W that significantly affects the

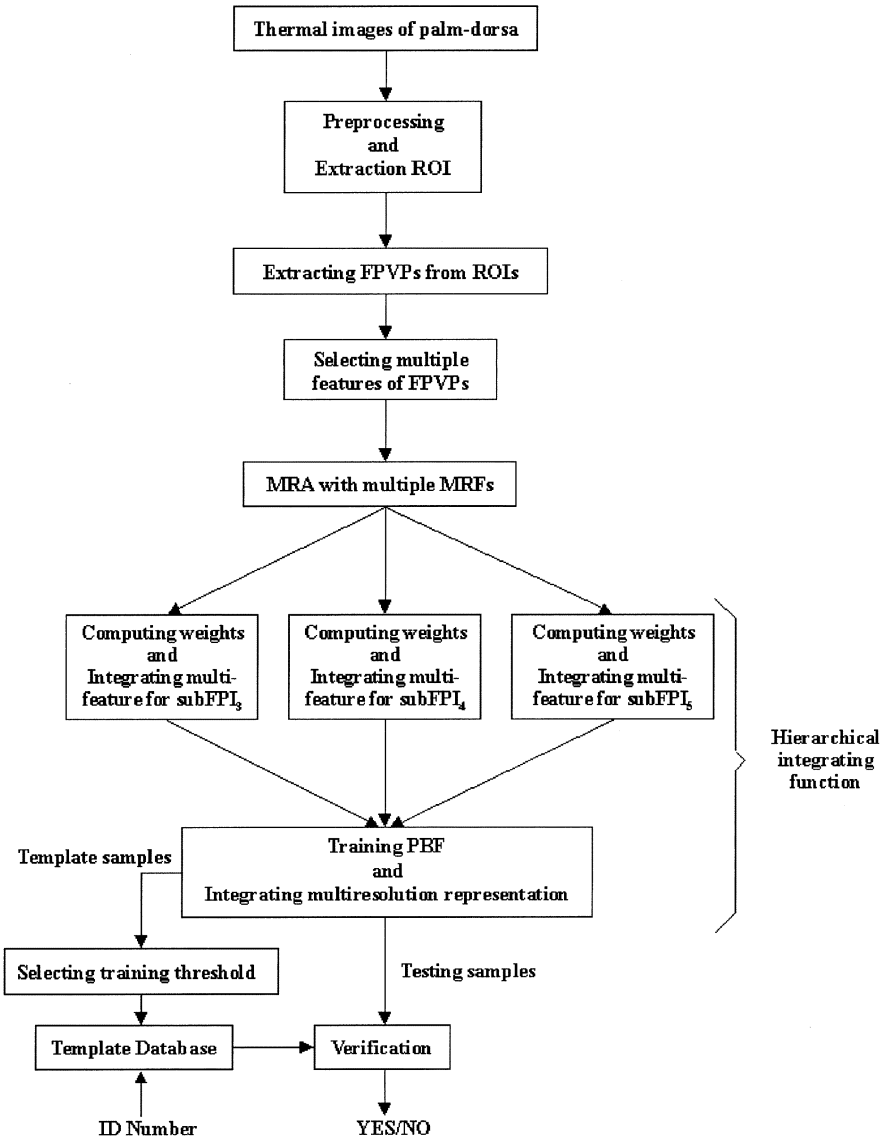

Fig. 1. Block diagram of the proposed approach.

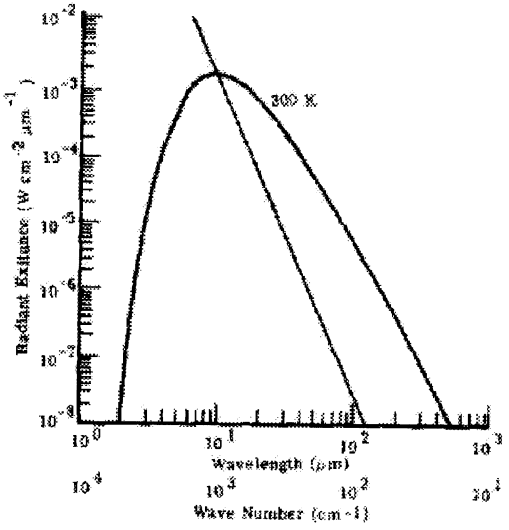

Fig. 2. Planck curve: spectrum radiant emittance versus wavelength.

thermal image contrast and quality. If the sensitive spectrum of an IR camera is 3–5 or 8–14 μm, the captured thermal images will be absolutely independent of visible light which is with a spectrum at 0.4–0.7 μm. Thus, the effects of unwanted skin surface features caused by visible light can be avoided to reduce the complexity of thermal images. In addition, the thermal images are robust under a wide range of lighting conditions. Thermal images of the palm-dorsa exhibit high contrast and are easily processed for verification, as shown in Fig. 4. However, there are still some factors that will affect the distinctiveness of the vein pattern, such as the thickness of the skin, the degree of venous engorgement, the condition of the vein walls, and the nearness of the vein to the surface [20].

The IR camera applied to capture thermal images was an InfraCam that is produced by the Inframetrics Corp. The specifications of InfraCam are described as follows:

Detector: PtSi 256 $\times$ 256 element FPA
IR wavelength: 3.4–5 μm

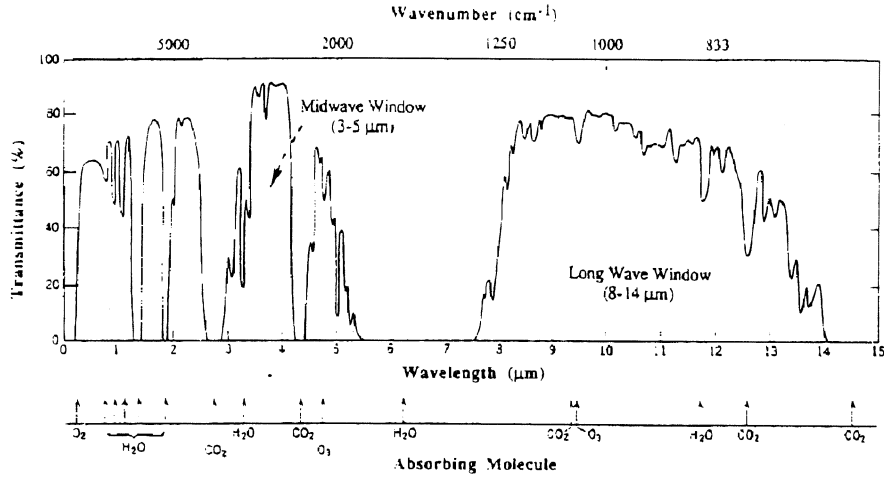

Fig. 3. IR transmission spectrum of the atmosphere for a 1.8-km horizontal path at sea level with 40% relative humidity.

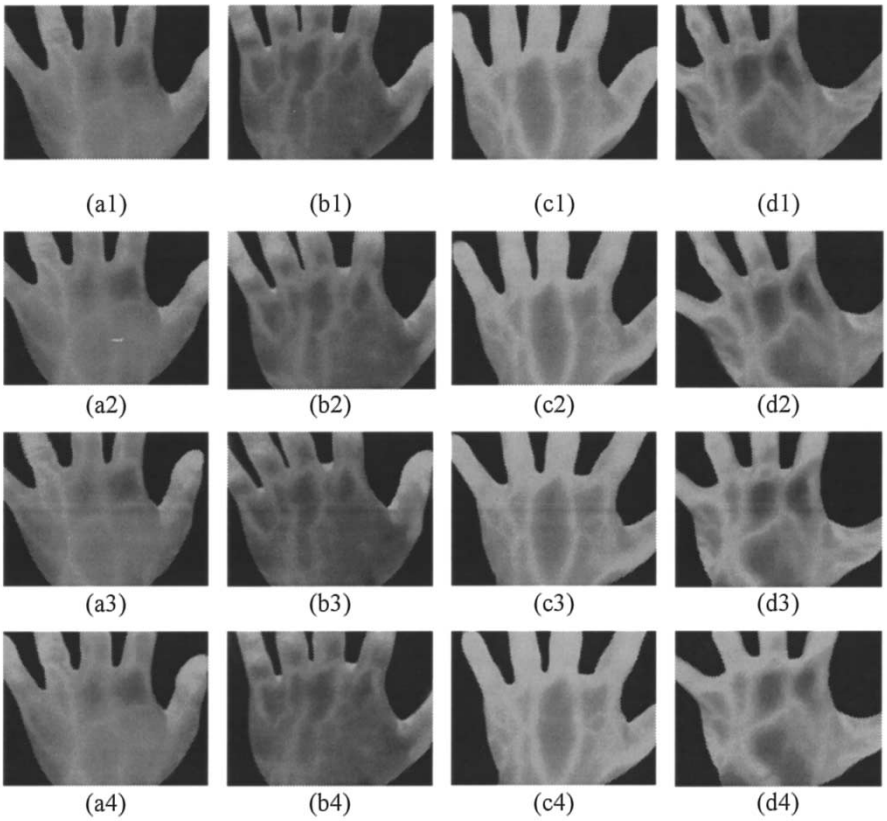

Fig. 4. Thermal images captured from four different palm-dorsa: (a1–a4), (b1–b4), (c1–c4), and (d1–d4).

NETD: 0.07 °C at 23 °C ambient temperature.
FOV: $8° \times 7°$.
MRT: 0.05 °C at 0.5 cycle/mrad.
Output: RS-170 TV format.

The IR camera outputs an analog image signal. Since computers do not accept analog signals, a frame grabber is needed to capture the thermal images for computer processing. The thermal image was digitized into 640×480 pixels with a grayscale resolution of 8 b per pixel. In order to verify the validity of the proposed approach, 960 thermal images of palm-dorsa are collected as the database in our study. They were captured from 32 volunteers, with 30 thermal images of each volunteer. The volunteers include three female and 29 male adults. To obtain high verification accuracy, it is important to construct an objective verification database. Therefore, we captured thermal images at three different times with each at an interval of at least one week. A total of 10 thermal images were acquired each time. In addition, the thermal images were captured under random light conditions, even in a dark environment without any light source. Thus, the database includes the variations of thermal images under various conditions. Each thermal image has a size of 640×480 and 256 gray levels.

III. Preprocessing and Extraction of the ROI

As shown in Fig. 4, thermal images with little noise were captured by the IR camera. The familiar median filter can be effectively utilized to reduce noise.

To increase the verification accuracy and reliability, the features of vein patterns extracted from the same region in different thermal images of the palm-dorsa are compared for verification. The region to be extracted is known as the ROI. For this reason, it is important to fix the ROI to be in the same position in different palm-dorsum images to ensure the stability of the principal extracted vein features. It also has significant influence on the accuracy of verification. However, it is difficult to fix the ROI at the same position in different palm-dorsum images without using a docking device to constrain the palm position. In our previous work [21], we selected the second and fourth finger webs as the datum points to define the ROI. The two finger webs can substitute for docking devices and determine the approximate (not absolute) immovable ROI, thus reducing the displacement of the ROI to an acceptable range in palm-dorsum thermal images. The procedures are stated as follows.

Step 1) Adopt the mode method in [22] to automatically determine the threshold for the segmentation of the palm region.

Step 2) Use the inner border tracing algorithm [22] to find the palm border.

Step 3) Locate the middle point of the intersection line that is formed by the wrist and the bottom margin of the thermal image of the palm-dorsum.

Step 4) Compute the Euclidean distance between each border pixel and the wrist middle point. These distances are adopted to construct a distance distribution diagram whose shape is quite similar to the geometric shape of a palm.

Step 5) Apply wavelet transformation to determine the four local minimums of the distance distribution diagram. They are the locations of the four finger webs.

Step 6) Select the second and fourth finger webs as the datum points to define a square ROI.

The details of the procedures can be found in [21]. Fig. 5 demonstrates the flowchart and illustrative example to show the procedures of how to determine the ROI. The ROIs extracted from different images of the same palm-dorsum are shown in Fig. 6. They cover almost the same region in different images captured from the same palm-dorsum.

IV. Feature Points and Multiple Features Extraction

Biometric verification based on a single feature does not yield a very low error rate. In order to further reduce the error rate, many researchers have turned their attention to the use of multifeature verification. Several interesting references in the literature [23]–[25] discussing this topic have been published and good results have been achieved. In this paper, we also extract multiple features to decrease the verification error rate.

The first law as stated in (1) reveals that the temperature T of the skin surface is the only variable which dominates the contrast and quality of thermal images. Moreover, heat conduction affects the temperature distribution on the skin surface. According to the Fourier law

$$Q_l = -kA\left(\frac{dT}{dl}\right) \tag{2}$$

where Q_l is the rate of heat flow through area A in the positive l direction, and constant k is the thermal conductivity of the material, the temperature gradient will vary over the same object surface. The temperature gradient direction changes slowly from high to low. This heat conduction law (2) means that the rate of heat flow due to conduction in a given direction is proportional to the area and the temperature gradient in that direction.

A. Feature Points Extraction

A healthy person free of fever or inflammation will have a steady temperature state, which means that the rate of heat flow Q_l is constant. The composition of the skin varies slightly, and this variation can be ignored. Thus, the thermal conductivity k is constant for an individual. The skin thickness for the same palm-dorsum does not vary over a short time. Hence, the area A can also be assumed to be constant. The temperature gradient and gradient direction can therefore be determined by the temperature T and the distance l. Based on the Stefan–Boltzmann law, the temperature T of the skin surface dominates the radiation emittance W. The IR camera will exhibit the received radiation emittance as the gray values in the thermal images. Thus, the skin surface temperature T significantly dominates the thermal image quality. The effects of unwanted skin surface features caused by visible light can now be avoided to reduce the complexity of the thermal images. The thermal images are also robust under a wide range of lighting conditions. In principle, the temperature varies smoothly over the same object surface, except for heat-insulating materials, which means that the temperature gradient is not large, especially for poor heat-insulating materials. The human body consists of about 70%–75% water and can thus be treated as a poor heat insulator because water is a poor heat insulator. By observing the thermal images of the palm-dorsa, we note that the gray level of the thermal images changes smoothly from a high to low temperature, as shown in Fig. 7(a). This means that the temperature gradient in the thermal images also changes smoothly. This observation conforms to the Fourier law that the magnitude of the temperature gradient is small. According to the observation, the familiar edge detectors based on gradient magnitudes, such as wavelet transformations, gradient operators, and Laplacian and morphological operators, cannot effectively extract the FPVPs from palm-dorsum thermal images. In addition, the feature points extracted from vein patterns by edge detectors are located at the edges of the veins, not at their actual locations. The FPVPs extracted via wavelet transformation with Daubechies 1 (db1) are shown in Fig. 7(b). In the figure, the feature points are superimposed on the corresponding ROI, which demonstrates that the feature points extracted by wavelet transformation are located at the edges of veins. By analyzing thermal images, the gray value of the veins is higher than that of the surrounding skin under normal conditions. Based on this analysis, we modify the basic tool for watershed transformation [26] in order to extract

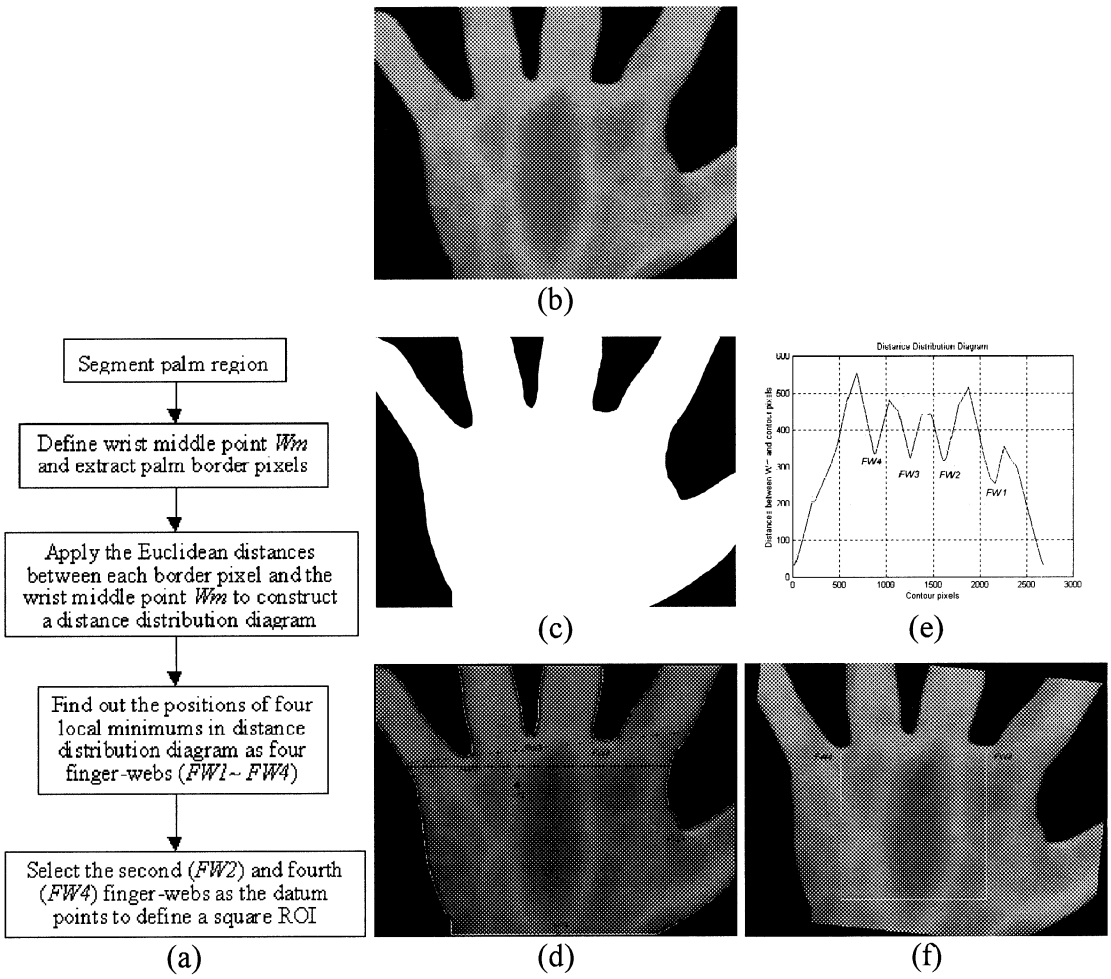

Fig. 5. Flowchart and illustrative figures to show the procedures of how to determine the ROI. (a) The flowchart of how to determine the ROI. (b) The original thermal image of the palm-dorsum. (c) The palm region is segmented by the mode method and transferred to binary image. (d) The palm border pixels (white points) are extracted by the inner border tracing algorithm. They are superimposed to the palm image to demonstrate that they match the palm region very well. (e) The Euclidean distance between each border pixel and the wrist middle point W_m is computed in sequence. These distances are applied to construct a distance distribution diagram. The positions that possess local minimums in the diagram are the finger webs $FW1 - FW$. (f) To define a square ROI, rotate the palm α to let the second $(FW2)$ and fourth $(FW4)$ finger webs be located on the horizon. The second and fourth finger webs are applied as the datum points to define a square ROI.

the FPVPs more effectively. The basic tool for watershed transformation is called the region maximum in [26], which can select pixels with a high gray value within a region as the candidates for watershed points. Here, the region maximum method is applied to extract the FPVPs, with two extra restrictions being added. One is that the pixel with a high regional maximum value is also the central point of the region. Another is that its gray value must be larger than the mean of the pixel value inside the region. The modified basic tool for watershed transformation is called the modified region maximum which can be stated as follows.

1) Function $f{:}Z^2 \rightarrow Z$ where $f(x,y)$ is the gray value of pixel (x,y).
2) The topographic surface S is the set of all pixels $\{(x_i,y_i), f_i(x_i,y_i)\}$ belonging to $Z^2 \rightarrow Z$.
3) A path between $s_1((x_1,y_1), f(x_{1i},y_1))$ and $s_2((x_2,y_2), f(x_2,y_2))$ is any sequence $\{s_i\}$ of S with s_i adjacent to s_{i+1}. S_{ri} is the region surrounding s_i
4) $M = \{s_i | \forall\, s_i, s_j \in S_{ri}$, if $i \neq j \leftrightarrow f_i \geq f_j$ where f_i is the center of S_{ri} and f_i is larger than the mean of $S_{ri}\}$.
5) The set M of all the regional maxima for f contains the feature points that compose the vein patterns.

The images that only include FPVPs are named feature point images (FPIs). Fig. 8 shows the FPIs superimposed on the corresponding original ROIs to confirm the location of FPVPs and vein patterns. The white points in Fig. 8 represent the FPVPs. These results demonstrate that this algorithm can efficiently extract FPVPs such that the verification rate based on the FPVPs is improved.

B. Multiple Features Extraction

Once the FPVPs have been correctly determined, intuitively, the feature number of the FPVPs inside the FPI will be larger, so the verification rate will be higher. It is very important to select the features representing the FPVPs. Based on the Fourier law, the FPVP locations, gray values of the FPVPs, and the distance between the FPVPs determine the temperature gradient and the gradient direction. Therefore, the x and y coordinates, the gray values, the temperature gradient, and the gradient direction of

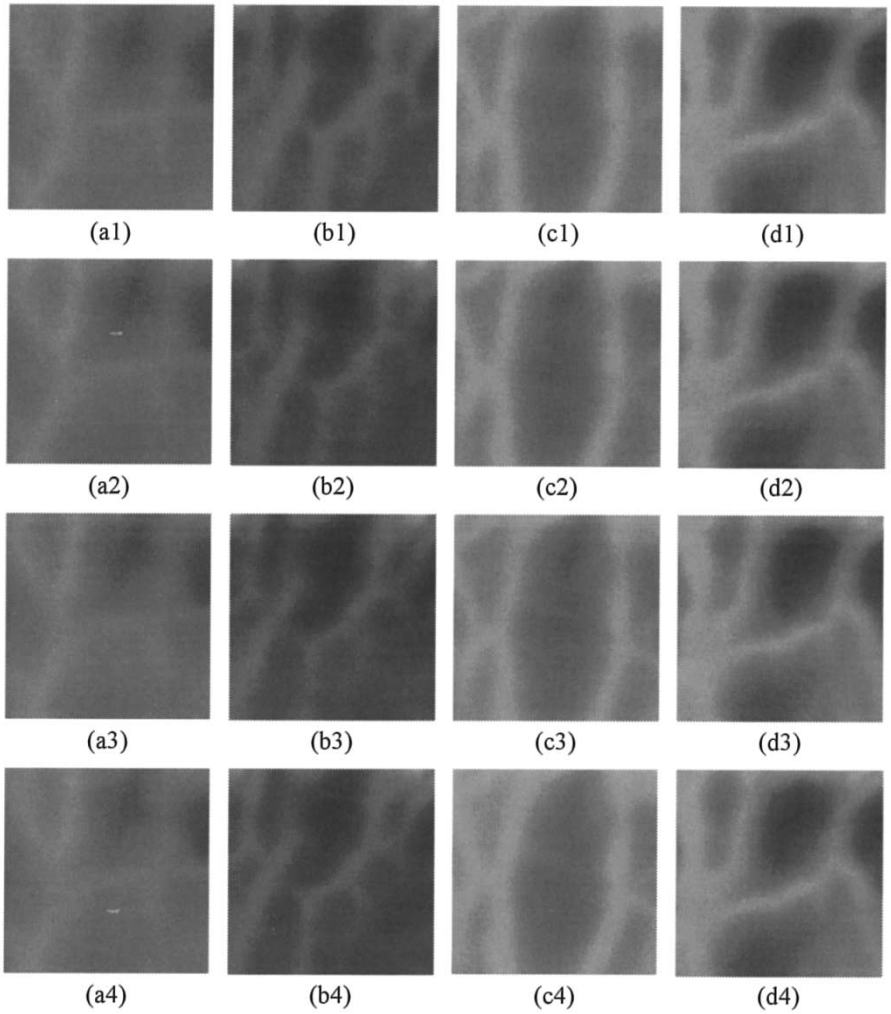

Fig. 6. ROIs extracted from different images in Fig. 4. They cover almost the same regions in different images of the same palm-dorsum.

the FPVPs are selected as the features. The feature vector is denoted as FV and is given as follows:

$$\mathrm{FV}(x,y) = [\,x \quad y \quad I \quad G \quad \theta \quad FP_N\,] \tag{3}$$

where x and y are the coordinates, $I = f(x,y)$ is the gray value, $G = [(\partial f/\partial x)^2 + (\partial f/\partial y)^2]^{1/2}$ is the temperature gradient, $\theta = \tan^{-1}[(\partial f/\partial y)/(\partial f/\partial x)]$ is the gradient direction, and FP_N is the FPVP's number. If (x,y) is an FPVP, then $\mathrm{FP}_N(x,y) = 1$, otherwise, $\mathrm{FP}_N(x,y) = 0$ in the FPIs.

V. Multiresolution Analysis and Multiresolution Representation

As we know, it is difficult to analyze the information content of an image merely from the gray-level intensity of the image. Local variations of the image intensity are more important. A multiresolution representation provides a simple hierarchical framework for interpreting image information [27]. At different resolutions, the information about an image generally represents different physical structures in the image. Many papers [7], [28]–[30] have discussed the application of multiresolution representations in image analysis.

Although the ROI has been carefully located according to the finger webs, it still cannot ensure that the ROI will always be located in the same position in different palm-dorsum thermal images. To resolve this problem, MRA is applied to decompose the FPI into multiscale FPIs, which we call subFPIs in the following discussion. The finer resolution is similar to watching a nearby object which possesses detailed information. It is sensitive to disturbances and noise. On the other hand, a coarser resolution is similar to watching a far object which possesses gross information. It is less sensitive to disturbances and noise. Thus, the effects of ROI displacements in different thermal images can be reduced to a more acceptable degree in low-resolution images.

Many MRFs have been presented in the literature. They can be categorized into two groups [28]: linear filters and nonlinear filters. Linear filters were developed long ago which include Gaussian filters, Fourier transformations, and wavelet transformations. Recently, nonlinear filters have become popular for morphological operators. Both are used for analyzing the single feature, gray levels, of images. In addition, they directly discard the pixels while down sampling. If the discarded pixels happen to be feature points, this will unfortunately result in the loss of the significant information about the biometric features at the

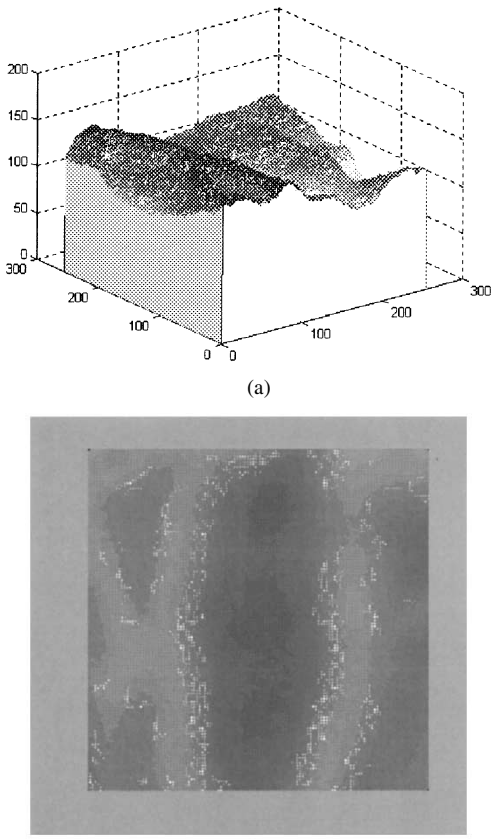

(a)

(b)

Fig. 7. (a) The temperature distribution shows that the temperature of thermal images varies smoothly. (b) Feature points (white points) extracted by wavelet transformation superimposed on the corresponding ROI show that they are located at the edges of the vein patterns and are unstable.

next-level resolution. To remedy this problem, we propose a novel approach to the MRA of FPIs using multiple MRFs.

Multiple features of FPVPs are extracted which possess different properties. While decomposing the FPI to the next level resolution, a single MRF cannot preserve all of the properties of the multiple features of each FPVP. Some information about the multiple features may be lost or decreased. In this paper, we propose the use of multiple MRFs to retain the properties of multiple features of the FPVPs at the next-level resolution while decomposing the FPIs. First, a novel MRF called a moment filter is employed. The moment is a well-known parameter that has been extensively applied to represent the features of objects in image processing. We apply it as an MRF to construct multiscale FPIs with the moments of intensity, gradient, and direction features and call it the moment filter in the following discussion. The moment filter can preserve the information about these three features of the FPVPs in FPIs while simultaneously reducing the resolution. However, it cannot attain this effectiveness for the x and y coordinates and the FP_N. Another MRF is needed to maintain the coordinate and FP_N information while reducing the FPI resolution. The second MRF is called a mean filter which computes the means of the x and y coordinate as representation for the next-level resolution. The mean filter preserves the locational information about FPVPs well. In addition, the number of feature points inside a local window is very important information which describes the significance of the vein pattern inside a local window. Since moment and mean filters are unsuitable for the FP_N, we propose using another MRF to count the FP_N inside the local square windows for representation of the next-level resolution, and we call it the counter filter. The three MRFs are described in Sections V-A–C.

A. Moment Filter

$$\mathrm{MDP}_I^{(m,n)}(p,q) = mom^n(\mathrm{FPVP}_w(x_i,y_i)), \quad i \in \{1,2,\ldots,2^m \times 2^m\} \tag{4}$$

where $\mathrm{MDP}_I^{(m,n)}(p,q)$ represents the nth moments of I at the mth level resolution whose coordinates are p and q, and $\mathrm{FPVP}_w(x_i,y_i)$ indicates the FPVPs inside a 2 m $\times$ 2 m window for the FPVP (x,y) in the original FPIs. In the same manner, $\mathrm{MDP}_G^{m,n}(p,q)$ and $\mathrm{MDP}\theta^{m,n}(p,q)$ are the nth moments of G and θ at the mth level resolution, respectively.

The moment operator $mom(ft)$ can be expressed as

$$mom^n(ft) = \sum_x \sum_y (x-\bar{x})^k (y-\bar{y})^l ft(x,y) \tag{5}$$

where $ft(x,y)$ represents the feature intensity, $n = (k+l)$ is the nth-order moment, and $\bar{x}$ and $\bar{y}$ are the mean values of the x and y coordinates, respectively.

B. Mean Filter

$$M_x(p,q)^{(m)} = mean(\mathrm{FPVP}_w(x_i,y_i)), \quad i \in \{1,2,\ldots,2^m \times 2^m\} \tag{6}$$

where $M_x(p,q)^m$ is the mean value of the x_i coordinates of $\mathrm{FPVP}_w(x_i,y_i)$ inside a 2×2 m^2 window in the original FPIs, and $M_y(p,q)^m$ represents the mean value of the y_i coordinates.

C. Count Filter

$$C_f^{(m)}(p,q) = count(\mathrm{FPVP}_w(x_i,y_i)), \quad i \in \{1,2,\ldots,2^m \times 2^m\} \tag{7}$$

where $Cf^m(p,q)$ is the number of $\mathrm{FPVP}_w(x_i,y_i)$ inside the $2^m \times 2^m$ windows and represents the number of FPVPs at the mth-level resolution.

Multiple MRFs, such as moment, mean, and counter filters, are utilized to process the original FPIs and to generate multiresolution representations. Each feature point in a multiresolution representation of an FPI possesses information about the number, location, intensity, gradient, and gradient direction of the FPVPs and includes the information about neighboring FPVPs at the last level resolution; these are called the *dominant points* in the following discussion. They can also help to reduce the data amount of template and decrease the computation load. For example, the dominant point can reduce 256×256 to 32×32, 16×16 and 8×8 at the third, fourth, and fifth levels, respectively. Multiple MRFs can extract the *dominant points* from the FPIs and construct the following new-resolution FPIs. In this paper, each original FPI is decomposed independently by

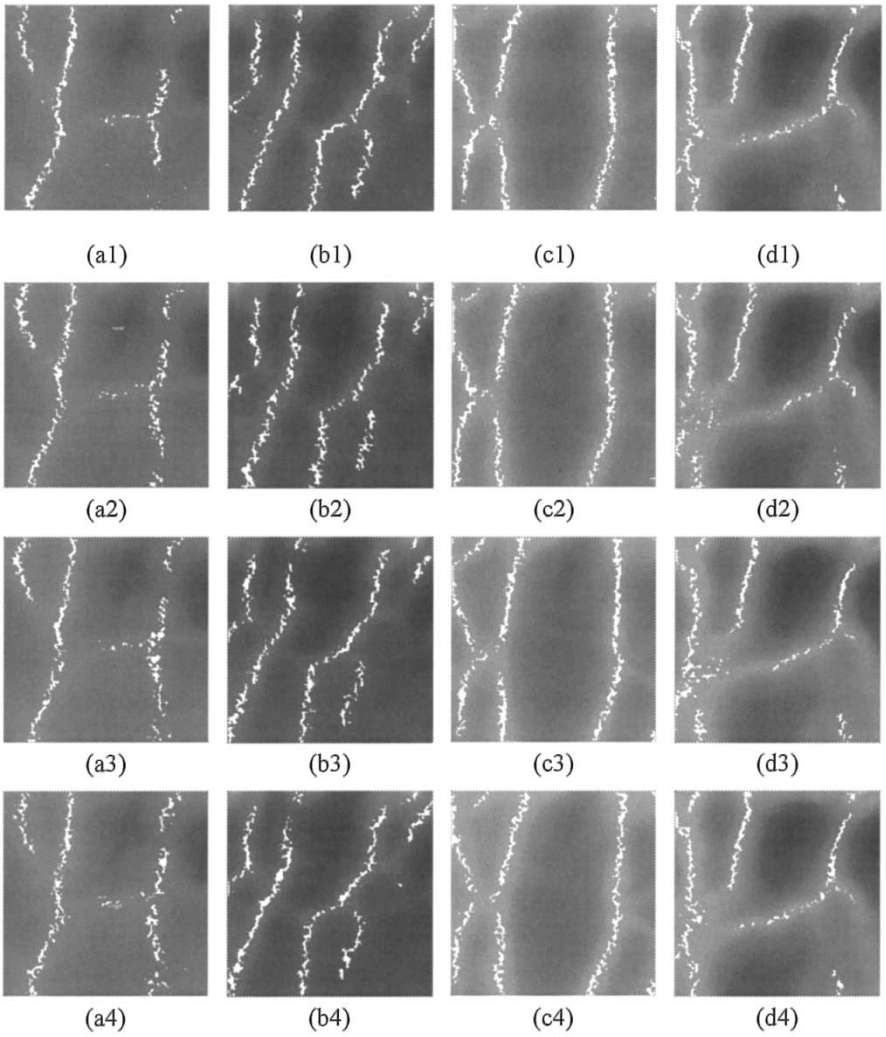

Fig. 8. FPIs generated from the ROIs in Fig. 4. They are superimposed on the corresponding ROIs to demonstrate the consistency between the FPVPs (white points) and the vein patterns.

the multiple MRFs into three resolutions with *dominant points* at the third, fourth, and fifth levels, called subFPI_3, subFPI_4, and subFPI_5, respectively. Fig. 9 shows the multiple features of *dominant points* at the third, fourth, and fifth levels that are obtained by applying multiple MRFs to filter the FPI of Fig. 8(a2).

VI. Design of an Integration Function

A. Integration Function for Multiple Features

In principle, if the number of features is larger, the information representing the object will be more. If the features are combined with a suitable method, the verification rate can be improved. Many literatures [23]–[25] have introduced multifeature applications to improve the accuracy of biometrics verifications. In this paper, we also extract multiple features from the FPVPs to increase the verification rate.

A crucial challenge for increasing the verification rate with multiple features is how to combine multiple features to obtain the maximum effect. Neural networks [25], [31]–[33] and fuzzy inference [8], [34] are the most familiar solutions for combining multiple features. Their validity for multifeature verification has been proven. In this paper, we adopt the properties of individual feature to combine multiple features. The properties are interobject distinctions and intraobject similarities. Therefore, we select weights based on these properties to combine the multiple features.

The weights should reflect the relative discriminating power of each feature. How to integrate multiple features is an issue in multifeature verification. One very difficult but important task is to determine an optimal weight for each feature. In order to achieve a high verification rate, the samples must possess distinctions between the inter-objects and similarities between the intra-objects. Thus, we adopt the inter-to-intra personal variation ratio of training samples to predict the efficacy of a feature representation for verification [29]. The applying of the inter-to-intra personal variation ratio WT as a weight matrix when integrating multiple features is defined as (see details in [35]) follows:

$$WT^{(m)} = \mathrm{tr}(Cm_{\mathrm{intra}^{-1}}^{(m)} Cm_{\mathrm{inter}}^{(m)}) \tag{8}$$

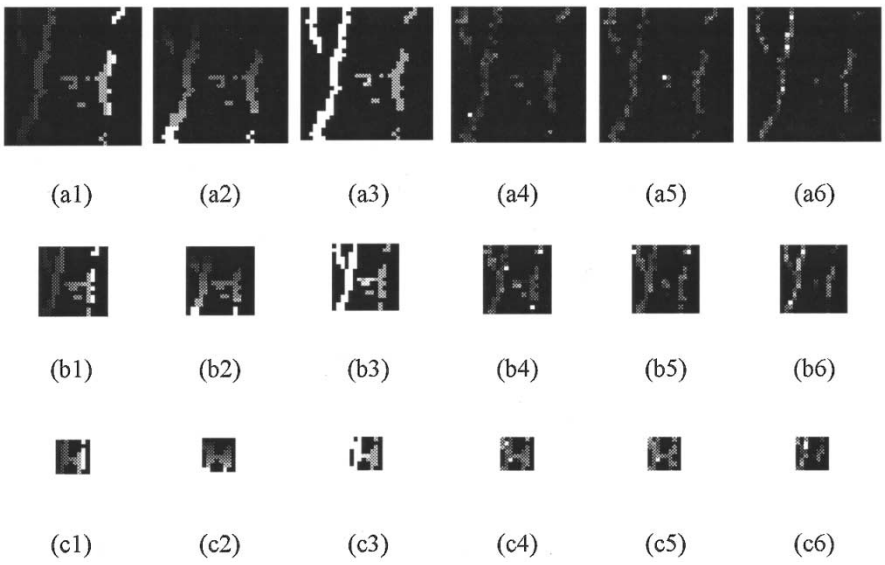

Fig. 9. Multiple features of dominant points at the third, fourth, and fifth levels that are obtained by applying multiple MRFs to filter the FPI of Fig. 8(a2). These figures are normalized in gray-level and magnified in scale for easy observation. (a1)–(a6) represent the features, x mean, y mean, I moment, G moment, θ moment, and FP_N count in the third level, respectively. Similarly, (b1)–(b6) and (c1)–(c6) show the filtered multiple features in the fourth and fifth levels, respectively.

$$Cm_{\text{intra}}^{(m)} = \left(\left(DP_{ij}^{(m)} - \overline{\mathrm{DP}}_i^{(m)}\right) \times \left(DP_{ij}^{(m)} - \overline{\mathrm{DP}}_i^{(m)}\right)^T\right) \tag{9}$$

$$Cm_{\text{inter}}^{(m)} = \left(\left(\overline{\mathrm{DP}}_i^{(m)} - \overline{\mathrm{DP}}_i^{(m)}\right) \times \left(\overline{\mathrm{DP}}_i^{(m)} - \overline{\mathrm{DP}}^{(m)}\right)^T\right) \tag{10}$$

where m represents the mth resolution, Cm_{intra}^{m} is the average intrapersonal covariance matrix of multiple features of the *dominant points* at the mth resolution, Cm_{inter}^{m} is the interpersonal covariance matrix of multiple features of the *dominant points* at the mth resolution, $WT^m = [wt_1^m \quad wt_3^{(m)} \quad wt_3^{(m)} \cdots wt_{nl}^{(m)}]^T$, and nl is the number of palm-dorsa in the database. DP_{ij}^{m} denotes the *dominant points* at the mth resolution of the jth thermal image of the ith palm-dorsum, and $\overline{\mathrm{DP}}_i^{(m)}$ and $\overline{\mathrm{DP}}^{(m)}$ represent the intrapersonal and overall means of the *dominant points* $\mathrm{DP}_{ij}^{(m)}$. If we assume $wtn_i^{(m)}$ to be the normalization of $wt_i^{(m)}$, then $wtn_i^{(m)}$ is the weight vector of the ith palm-dorsum. Thus, $|wtn_i^{(m)}| = 1$ and $wtn_i^{(m)} = [w_x^{(m)} \quad w_y^{(m)} \quad w_i^{(m)} w_g^{(m)} w_\theta^{(m)} w_{fpn}^{(m)}]$, $w_x^{(m)}$, $w_y^{(m)}$, $w_i^{(m)}$, $w_g^{(m)}$, $w\theta^m$, and $w_{\text{fpn}}^{(m)}$ are the weights of x, y, I, G, θ and FP_N, respectively. Each palm-dorsum has an individual weight vector based on the properties of its multiple features.

The integrated value $\mathrm{IVD}_i^{(m)}$ of the multiple features of the *dominant points* of the ith palm-dorsum at the mth resolution can be expressed as follows:

$$\mathrm{IVD}_i^{(m)} = \mathrm{DV}_i^{(m)} \times wtn_i^{(m)T} \tag{11}$$

where wtn_i^m is the normalized weight vector of the ith palm-dorsum at the mth resolution, and $\mathrm{DV}_i m(p,q) = [M_x(p,q)^{(m)} M_y(p,q)^{(m)} \mathrm{MDP}_I^{m,n}(p,q) MDP_G^{m,n}(p,q) \quad \mathrm{MDP}\theta^{m,n}(p,q) \quad Cf^m(p,q)]$ is the feature vector of the *dominant points* of the ith palm-dorsum at the mth resolution.

B. Integration Function for MRA

A great deal of research has been conducted on MRA of images. Similar to multiple features application, MRA can produce more information than was available in the original images. The same question arises of how to integrate the multiresolution representations obtained by MRA. Many published papers have integrated MRA with neural networks [29], [31] and yielded good results. Here, we propose a novel approach, the PBF, to integrate the multiresolution representations of the palm-dorsum thermal images generated by MRA.

The PBF has been successfully applied to the analysis of stack filter. Each stack filter corresponds to a PBF. There are many familiar types of stack filters that have been developed. They include median filters, weighted median filters, order statistic filters, weighted order median filters, and so on. A great amount of the literature has focused on their main application in image and signal processing, such as edge detection [36]–[38] and noise removal [39].

The main advantage of the PBF is that it is possible to design the optimal filter for reducing a variety of noise distributions and preserve the edge information or image detail. A PBF can be designed with only a few positive training samples or even one positive sample. Another crucial advantage is that the PBF can be realized in parallel very large scale integration for real-time application. There are two merits of applying the PBF to integrate MRA. First, it can alleviate the disadvantage of the MRA approach, which is that a relatively complex decision rule must be synthesized [29]. Second, we can avoid the shortcoming of relying on neural networks to integrate MRA that needs abundant positive and negative training samples [6], [25], [31], [32]. In this paper, we adopt PBFs to combine the MRA based on its need for few positive training samples, noise removal, and

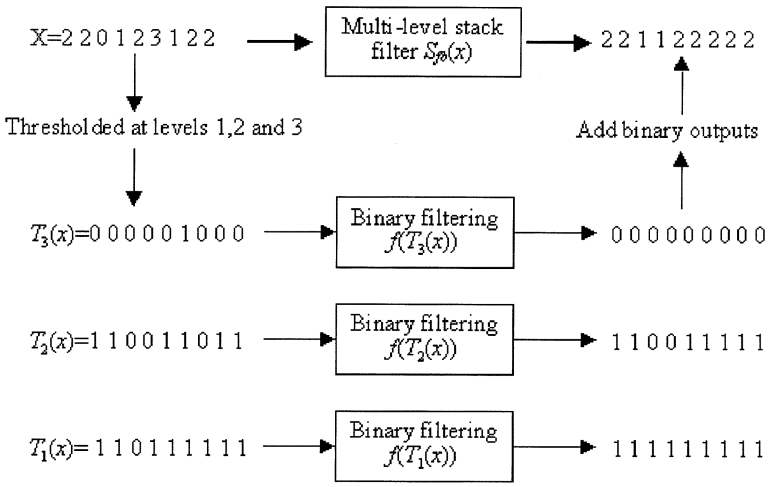

Fig. 10. Threshold decomposition and stacking properties of stack filters. The multilevel stack filter S_{fb} is specified by the PBF $f(x_1, x_2, x_3) = x_1x_2 + x_1x_3 + x_2x_3$. The input multilevel signal X is thresholded into binary signals. The binary filter operation defined by the PBF is performed on all binary thresholded signals. The result of multilevel stack filtering can be obtained by summing up all of the binary filter outputs. The stacking property of thresholded binary signals is preserved after the binary filtering of a PBF.

the capability of preserving image details. The template samples can be regarded as the original signals or images. Positive training samples and positive testing samples can be treated as noisy original signals which will closely approximate the original signals if processed by the PBF. The PBF can reduce the differences caused by noise and maintain the same major vein-pattern structures between noisy images and the original images captured from the same palm-dorsum. On the other hand, it may also decrease the noise in different images but not be that significant in dominant vein-pattern structures of different palm-dorsa.

The PBF possesses two well-known important properties. One is the threshold decomposition property, and the other is the stacking property. These two properties can be succinctly and obviously demonstrated by the example [40] shown in Fig. 10. The first is the threshold decomposition property. The multilevel stack filter can be realized by operating a PBF on thresholded binary images due to the threshold decomposition property

$$Th_k(x_i) = \begin{cases} 1, & x_i \geq k \\ 0, & x_i < k \end{cases} \tag{12}$$

$$S(X) = \sum_{k=1}^{M-1} S[TH_k(X)] \tag{13}$$

where Th is the threshold function, $X = \{x_1, x_2, \ldots, x_n\}$ is a grayscale vector with length n, $Th_k(x_i)$ is the element x_i of the X thresholded at threshold level k, S is a filter with the threshold decomposition property, $Th_k(X)$ is the thresholded binary vector with threshold level k, and $S[Th_k(X)]$ is the output of the filter S operating on a binary vector $Th_k(X)$

The second is the stacking property. The stacking property is sufficient to ensure that stack filters have the threshold decomposition property. The reason is that stack filters can be specified by PBFs and operated as a combination of local min and max operations [41] as follows:

$$S(P) \geq S(Q) \text{ whenever } p \geq Q$$

where $P = (P_1, P_2, \ldots P_n)$ and $Q = (Q_1, Q_2, \ldots Q_n)$ are two multilevel vectors.

The procedures for designing an optimal stack filter are described as follows [40].

Step 1) Generate a Hasse diagram with 2^n vertices, where n is the window size of the stack filter.

Step 2) Estimate the cost coefficient of each vertex according to the statistical measurement between the template samples and the training samples. A fast algorithm for computing the cost function is described in detail in [42]. Let $b = (x_1, \ldots, x_n)$ be an input window vector, z is the desired output of the filter for input vector b, M is the largest gray level of the input signal, n is the window size, and $T_{km}(z)$ is the thresholded binary vector of z at threshold level k_m

a) Sort the n elements of input vector b and the desired output z. The ordered $n+1$ elements are put into a vector $K[n+1] = \{k_1, k_2, \ldots, k_{n+1}\}$, where $k_1 \leq k_2 \leq \cdots \leq k_{n+1}$.

b) The cost coefficient can be computed by $C(T_{km}(z), T_{km}(b)) = k_m - k_{m-1}$, for $m = 1$ to $n+1$, where the initial conditions are $k_0 = 0$ and $C(0,0) = M - k_n$.

c) As the window slips through the entire signal, the cost coefficient of an input vector b can be defined by the cost $(b) = C(0,b) - C(0,b)$, where $C(0,b)$ is estimated by the number of occurrences of an input vector b which appears in the observed signal when the desired output of its vector is 0. Likewise, $C(1,b)$ is estimated by the number of occurrences of an input vector b which appears in the observed signal when the desired output of its vector is 1.

Step 3) An efficient algorithm to find the optimal onset under the mean absolute error (MAE) criterion has been developed by Lee and Fan [40]. The mean absolute error (MAE) is defined as the mean absolute difference between the desired signal Z and the output of a stack filter with the observed signal X serving as the input

$$MAE(S_{fb}) = E[|Z - S_{fb}(X)|]. \tag{14}$$

where S_{fb} is a stack filter, fb is the PBF that defines the Boolean algebra of the stack filter.

In this way, the optimal onset can be found and the corresponding PBF can be easily determined. The applying of PBFs in combining the MRA has a special property that does not need negative training samples to train (design) the PBF for each person. Thus, the number of necessary training samples can be reduced and the training time can thereby be decreased.

In order to implement PBF to filter three different dimensional sub-FPIs (subFPI_3, subFPI_4 and subFPI_5) of a palm-dorsum thermal image, we reshape each two-dimensional sub-FPI to a one-dimensional row and join them together in one concatenate row vector. The row vector represents each palm-dorsum thermal image which can be seen as a signal vector and filtered by the corresponding trained PBF. Then, compute the MAE between the output of PBF and the desired signal vector that represents the template thermal image. The MAE can be utilized as a criterion to judge whether the test sample is accepted or rejected.

VII. Selecting the Trained Threshold

As we know, image segmentation is a very important task in image processing. The threshold significantly affects the performance of image segmentation. Abundant research has been conducted on the method of threshold selection for image segmentation over the past decade. However, no one work elaborately considers a threshold selection method for verifications, even when the threshold significantly affects the verification results.

It does not matter if the outputs of the verification algorithm are similarities or distinctions between objects. Threshold selection requires a preset value to help discriminate the verifying object from the database. Hence, the threshold will influence the verification rate significantly. The selection of an optimal threshold to achieve a high verification rate is a very important but difficult task. In this paper, we propose a novel method to determine a near-to-optimal threshold to achieve a near-to-optimal verification rate.

The well-known statistical pair, the false rejection rate (FRR) and the false acceptance rate (FAR), is usually adopted to evaluate the verification performance. In our method, we also adopt them to determine the threshold. In the verification experiment, an FAR and an FRR based on positive and negative training samples are computed. The distinction or similarity threshold is set to be R. Shown in Fig. 11(a) are the FAR and FRR with various thresholds R. By observing Fig. 11(a), it is easy to find that the experimental results at the cross-over point of the FAR and FRR curves indicate the minimum verification error. We then select a threshold according to the minimum error in Fig. 11(a)

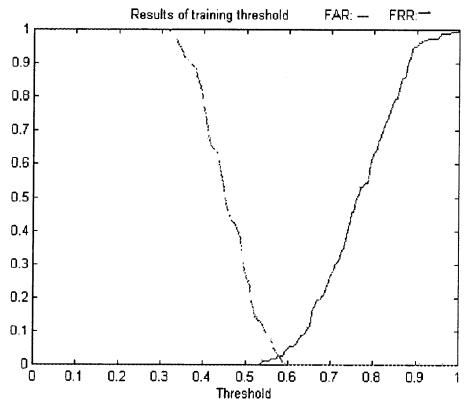

(a)

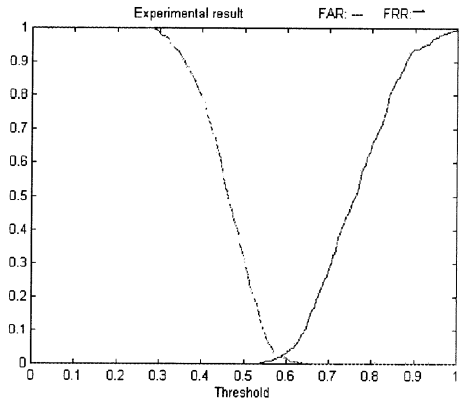

(b)

Fig. 11. (a) Selecting a trained threshold. Minimum error = 3.75% with threshold = 0.58 (near-to-optimal threshold). (b) Experimental results. Minimum error = 2.3% with threshold of 0.59; FRR is 1.5% and FAR is 3.5% with a near-to-optimal threshold of 0.58.

to verify the testing samples. The threshold is named near-to-optimal threshold which is selected as follows:

$$\mathrm{ERR}(R) = \max\{\mathrm{FAR}(R), \mathrm{FRR}(R)\} \tag{15}$$

$$\mathrm{ERR}_{\min} = \min\{\mathrm{ERR(R)}\} \tag{16}$$

$$R_{\mathrm{no}} = \{R | ERR(R) = \mathrm{ERR}_{\min}\} \tag{17}$$

where $\mathrm{FAR}(R)$ and $\mathrm{FRR}(R)$ are the error functions of FAR and FRR with the threshold R, respectively. $\mathrm{ERR}_{\min}$ is the minimum error rate at the crossover point. R_{no} is the threshold at the crossover point that is the near-to-optimal threshold which generates the minimum error rate based on the training samples.

A near-to-optimal threshold is selected based on the FAR and FRR curves. It is not guaranteed that a minimum error rate can be achieved for the testing samples. However, a near-to-minimum error rate can be achieved. In addition, the threshold selected by the proposed method is more logical and reasonable than that selected by the trial-and-error or intuition methods. It can effectively reduce the difficulties in selecting an optimal threshold and easily obtain a compromising near-to-optimal threshold.

VIII. Experimental Results

In this section, experimental results are illustrated to demonstrate the validity and efficiency of our proposed method in ver-

ifying the thermal images of palm-dorsa vein patterns. For each palm-dorsum in database, we use five images as template samples, five images as training samples to design PBF, five images as training samples to select a near-to-optimal threshold, and the other 15 images as testing samples to verify the performance of the proposed approach. Each thermal image in the database is transformed into an FPI according to the following procedures: defining a square ROI, extracting FPVPs from ROIs, and selecting multiple features from each FPVP. Each FPI is then decomposed into three scales, subFPI_3, subFPI_4, and subFPI_5, by multiple MRFs. Their sizes are 32×32, 16×16, and 8×8, respectively. The multiple features of *dominant points* in these three subFPIs are integrated with weights to obtain the integrated values.

We then serialize subFPI_3, subFPI_4, and subFPI_5 into three row vectors and link the three row vectors to form one row vector. The row vector represents each palm-dorsum thermal image for verification purpose and is called the *dominant point* row (DPR). Thirty DPRs of each palm-dorsum are categorized into four groups. Likewisely, five DPRs are used for template samples, five DPRs for PBF training samples, five DPRs for verification threshold selecting training samples, and the other 15 DPRs for testing samples.

In order to reduce the effects of noises and disturbances, the five template DPRs are averaged to form a template of each palm-dorsum. Then, we apply the five training DPRs to design a PBF for each person. The designed PBF slides through each verification threshold selecting a training DPR to generate an output and the MAEs are computed between the five outputs and the template. Similarly, a PBF is applied to slide through the negative verification threshold selecting training DPRs and compute the MAEs. These MAEs are used to select a near-to-optimal verification threshold and are assembled to form a set called MAE_{VT}. The FRR and FAR curves are constructed based on the MAE_{VT} with various threshold R as shown in Fig. 11(a). Then, select the near-to-optimal threshold based on (15)–(17) to verify the testing DPRs. Here, the selected near-to-optimal threshold is 0.58. In the same way, the testing DPRs are processed by PBF. The MAEs between the testing DPRs and the templates can also be computed. In order to distinguish them from MAE_{VT}, these MAEs are called $\mathrm{MAE}_{TST}s$. According to $\mathrm{MAE}_{TST}s$, the FRR and FAR curves are reconstructed as shown in Fig. 11(b). The threshold selection method is applied again based on (15)–(17) to determine the optimal threshold and the minimum error rate. They are 0.59 and 2.3%, respectively. By observing the FRR and FAR curves in Fig. 11(a), we can find that the near-to-optimal threshold is 0.58 and the corresponding error rate is 3.75%. By comparing the minimum error rate 2.3% and the error rate 3.75% caused by the near-to-optimal threshold, the difference is very small and is acceptable. The result demonstrates the validity of the proposed method in selecting the near-to-optimal threshold.

Failure verifications do occur in some palm-dorsum thermal images. They can be categorized into two main groups by carefully analyzing the failures.

1) A few palm-dorsum thermal images possess the rare constitution with the gray value of the vein patterns being lower than the surrounding skin as shown in Fig. 12(a). This phenomenon will generate the extracted feature points which do not indicate the vein patterns but skins with high gray values. If the skins with high gray values are stable in fixed regions, (i.e., the extracted feature points are stable), the palm-dorsa will be correctly verified. Otherwise, verifications may fail.
2) Most of the palm-dorsum thermal images that result in failure verifications have unobvious vein patterns as shown in Fig. 12(b). These may be due to thick subcutaneous fat of the palm-dorsa. The gray values of these images are nearly homogeneous and lack a stable fixed region with high contrasting gray values. Similar to group 1), it is not easy to extract the stable feature points of vein patterns. The extracted feature points will mostly be located at the position with high gray values and will be unstable. If feature points do not appear in the closely same position in the samples of the same palm-dorsum, it will also result in the failure verification.

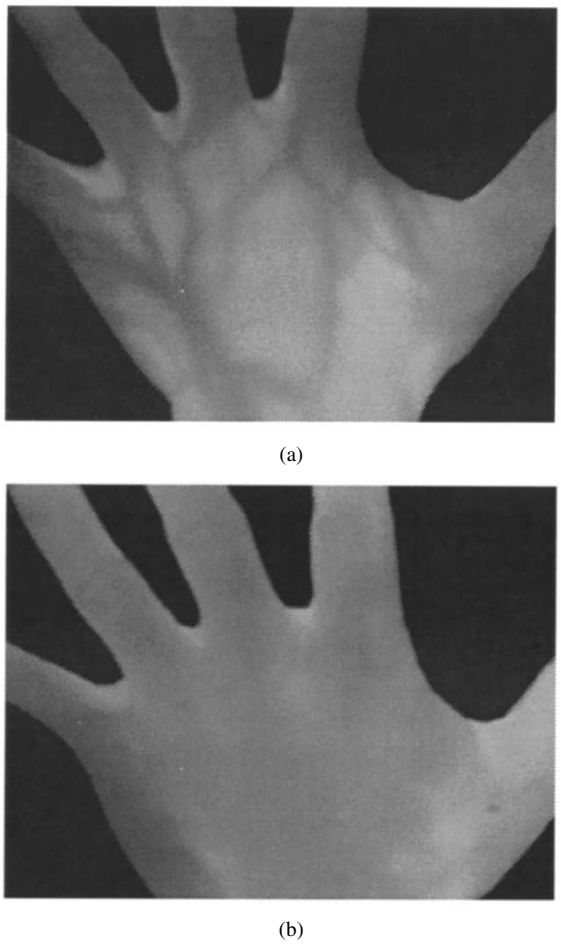

(a)

(b)

Fig. 12. Thermal images that result in verification failure: (a) the gray value of the vein patterns is lower than the surrounding skin and (b) the thermal palm-dorsum image has unobvious vein patterns.

It is difficult to distinguish the palm-dorsa in groups 1) and 2) as mentioned above with our approach. This problem can be alleviated by utilizing other methods to extract FPVPs, associating with other biometric features, combining other biometric verification methods, or capturing the thermal images with an IR camera that yields a more sensitive or wider spectrum response.

IX. Conclusion

The central problem in biometric verification is to find an efficient and effective approach which can characterize biometric features and measure the degree of similarity or distinction between two persons. In this paper, we propose a novel personal verification method based on the vein patterns of palm-dorsa. Unlike general biometric verification methods that need some preset parameters, our approach can set the parameters automatically. This paper demonstrates the advantages of our proposed approach by devising a multiple-features scheme, MRA with multiple MRFs, an inter-to-intra personal variation ratio, and a PBF integrating function for vein-pattern verification. In addition, the selection of a near-to-optimal threshold further improves the verification rate. Based on a limited database, a near-to-perfect verification rate is obtained.

There is still some work that requires further investigation to reduce the effects caused by the ambient temperature, the thickness of the overlapping skin, the degree of venous engorgement, the condition of the vein walls, and the nearness of the vein to the surface. Any variation in the surrounding temperature may lead to unstable distribution patterns of gray value in thermal images. This problem is very difficult to resolve by relying only on the vein-pattern features in palm-dorsum thermal images. One possible solution would be to combine vein patterns with other biometric features for verification. The other effects as mentioned above may cause the vein patterns to be unobvious. Their influences can be decreased by capturing the thermal images of palm-dorsa with an IR camera which possesses higher sensitivity or wider spectrum response. Moreover, the combining of vein patterns with other biometric features for verification would also provide effective solutions.

In addition, most biometric features of an individual will vary with age. The aging period is long and inevitable, and this fact cannot be avoided or neglected over a long time which might increase the error rate. To maintain long-term verification accuracy, this problem must be solved or alleviated. Since aging will occur in the future, the verification approach should be capable of predicting biometric feature variations so that the influence of aging can be reduced to the minimum. The Kalman predictor [43] is known to possess such prediction capabilities. One possible solution is to apply the Kalman predictor to predict the variations caused by aging and to modify the templates in the database.

References

[1] A. K. Jain, R. Bolle, and S. Pankanti, *Biometrics Personal Identification in Networked Society*. Boston, MA: Kluwer, 1999.

[2] Y. Yoshitomi, T. Miyaura, S. Tomita, and S. Kimura, "Face identification thermal image processing," in *Proc. 6th IEEE Int. Workshop Robot and Human Communication*, RO-MAN' 97 SENDAI, pp. 374–379.

[3] A. J. Rice, "A quality approach to biometric imaging," *Proc. Image Processing for Biometric Measurement IEE Colloq.*, pp. 4/1–4/5, Apr. 1994.

[4] J. M. Cross and C. L. Smith, "Thermographic imaging of the subcutaneous vascular network of the back of the hand for biometric identification," in *Proc. IEEE 29th Annu. Int. Carnahan Conf. Security Technology*, 1995, pp. 20–35.

[5] B. Miller, "Vital sign of identify," *IEEE Spectrum*, vol. 31, pp. 22–30, Feb. 1994.

[6] C. C. Han, H. L. Cheng, C. L. Lin, and K. C. Fan, "Personal authentication using palmprint features," *Patt. Recognit.*, vol. 36, no. 2, pp. 371–381, 2003.

[7] J. You, W. Li, and D. Zhang, "Hierarchical palmprint identification via multiple feature extraction," *Patt. Recognit.*, vol. 35, pp. 847–859, 2002.

[8] H. J. Lin, H. H. Guo, F. W. Yang, and C. L. Chen, "Handprint identification using fuzzy inference," in *Proc. 13th IPPR Conf. Computer Vision Graphics and Image Processing*, 2000, pp. 164–168.

[9] C. C. Han, P. C. Chang, and C. C. Hsu, "Personal identification using hand geometry and palm-print," in *Proc. 4th Asian Conf. Computer Vision (ACCV)*, 2000, pp. 747–752.

[10] A. K. Jain and N. Duta, "Deformable matching of hand shapes for verification," in *Proc. ICIP*, 1999, pp. 857–861.

[11] D. P. Zhang and W. Shu, "Two novel characteristics in palmprint verification: datum point invariance and line feature matching," *Patt. Recognit.*, vol. 32, pp. 691–702, 1999.

[12] D. G. Joshi, Y. V. Rao, S. Kar, V. Kumar, and R. Kumar, "Computer-vision-based approach to personal identification using finger crease patterns," *Patt. Recognit.*, vol. 31, pp. 15–22, 1998.

[13] S. K. Im, H. M. Park, S. W. Kim, C. K. Chung, and H. S. Choi, "Improved vein pattern extracting algorithm and its implementation," in *Int. Conf. Consumer Electronics Dig. Tech. Paper*, 2000, pp. 2–3.

[14] S. K. Im, H. M. Park, Y. W. Kim, S. C. Han, S. W. Kim, and C. H. Hang, "An biometric identification system by extracting hand vein patterns," *J. Korean Phys. Soc.*, vol. 38, pp. 268–272, Mar. 2001.

[15] A. J. Mehnert, J. M. Cross, and C. L. Smith, "Thermalgraphic Imaging: Segmentation of the Subcutaneous Vascular Network of the Back of the Hand (Research Report)," Edith Cowan University, Australian Institute of Security and Applied Technology, Perth, Western Australia, 1993.

[16] H. Kuno and S. Kougaku, *IEICE Trans.*, Japanese, 1994, pp. 22–22.

[17] E. F. Godik and Y. V. Guljaev, "Functional imaging of the human body," *IEEE Trans. Eng. Med. Biol.*, vol. 10, pp. 21–29, Apr. 1991.

[18] W. L. Wolfe and G. J. Zissis, *The Infrared Handbook*. Washington, DC: ONR, 1978.

[19] D. C. Harris, *Infrared Window and Dome Materials*. Bellingham, WA: SPIE, 1992.

[20] A. A. Newman, Ed., *Photographic Techniques in Scientific Research*. London, U.K.: Academic, 1976, vol. 2.

[21] C. L. Lin, K. C. Fan, and F. D. Chou, "A novel approach to palmprint verification utilizing finger-webs as datum points," *Image Vis. Comput.*, submitted for publication.

[22] M. Sonka, V. Hlavac, and R. Boyle, *Image Processing, Analysis, and Machine Vision*, 2nd ed. New York: PWS, 1999.

[23] F. Kimura and M. Shridhar, "Handwritten numeral recognition based on multiple algorithms," *Patt. Recognit.*, vol. 24, pp. 976–983, 1991.

[24] S. N. Shridhar, "Recognition of handwritten and machine printed text of postal address interpretation," *Patt. Recognit. Lett.*, vol. 14, pp. 291–302, 1993.

[25] J. Cao, M. Ahmadi, and M. Shridhar, "Recognition of handwritten numerals with multiple feature and multistrage classifier," *Patt. Recognit.*, vol. 28, pp. 153–160, 1995.

[26] S. Beucher, "The watershed transformation applied to image segmentation," in *Proc. 10th Pfefferkorn Conf. on Signal and Image Processing in Microscopy and Microanalysis*, Cambridge, U.K., Sept. 16–19, 1991, pp. 299–314.

[27] J. koenderink, "The structure of images," in *Biological Cybernetics*. New York: Springer-Verlag, 1984.

[28] Y. Shinagawa and T. L. Kunil, "Unconstrained automatic images matching using multiresolutional critical-point filter," *IEEE Trans. Pattern Anal. Machine Intell.*, vol. 20, pp. 994–1010, Sept. 1998.

[29] Y. Qi and B. R. Hunt, "A multiresolution approach to computer verification of handwritten signatures," *IEEE Trans. Image Processing*, vol. 4, pp. 870–874, June 1995.

[30] J. You and P. Bhattacharya, "A wavelet- based coarse-to-fine image matching scheme in a parallel virtual machine environment," *IEEE Trans. Image Processing*, vol. 9, pp. 1547–1559, June 2000.

[31] K. Huang and H. Yan, "Off-line signature verification based on geometric feature extraction and neural network classification," *Patt. Recognit.*, vol. 30, pp. 7–17, 1997.

[32] G. Y. Chen, T. D. Bui, and A. Krzyzak, "Contour-based handwritten numeral recognition using multiwavelets and neural networks," *Patt. Recognit.*, vol. 36, pp. 1597–1604, 2003.

[33] K. Huang and H. Yan, "Signature using multiple neural classifiers," *Patt. Recognit.*, vol. 30, pp. 1–7, 1997.
[34] M. A. Ismail and S. Gad, "Off-line arabic signature recognition and verification," *Patt. Recognit.*, vol. 33, pp. 1727–1740, 2000.
[35] K. Fukunaga, *Introduction to Statistical Pattern Recognition*, 2nd ed. New York: Academic, 1972.
[36] P. S. Wu and M. Li, "Pyramid edge detection based on stack filter," *Patt. Recognit. Lett.*, vol. 18, pp. 239–248, 1997.
[37] J. Yoo, E. J. Coyle, and C. A. Bouman, "Dual stack filters and the modified difference of estimates approach to edge detection," *IEEE Trans. Image Processing*, vol. 6, pp. 1634–1645, Dec. 1997.
[38] J. Yoo, C. A. Bouman, E. J. Delp, and E. J. Coyle, "The nonlinear prefiltering and difference of estimates approaches to edge detection: Application of stack filters," *CVGIP: Graph. Models Image Process.*, vol. 55, Mar. 1993.
[39] P. T. Yu and R. C. Chen, "Fuzzy stack filters- their definitions, fundamental properties and application in images processing," *IEEE Trans. Image Processing*, vol. 5, pp. 838–854, Dec. 1996.
[40] W. L. Lee and K. C. Fan, "Design of optimal stack filter and under MAE criterion," *IEEE Trans. Signal Processing*, vol. 47, pp. 3345–3355, Dec. 1999.
[41] Y. Nakagawa and A. Rosenfeld, "A note on the use of local min and max operations in digital picture processing," *IEEE Trans. Syst., Man Cybern.*, vol. SMC-8, pp. 632–635, Aug. 1978.
[42] C. C. Han, K. C. Fan, and Z. M. Chen, "Finding of optimal stack filter by graphic searching method," *IEEE Trans. Signal Processing*, vol. 45, pp. 1857–1862, July 1996.
[43] S. M. Bozic, *Digital and Kalman Filtering*. New York: Edward Arnold, 1979.

Chih-Lung Lin was born in Tainan, Taiwan, on January 15, 1965. He received the B.S. degree in automatic control engineering from Feng-Chia University, Taichung, Taiwan, in 1987, the M.S. degree in electronics engineering from Chung Cheng Institute of Technology, Taoyuan, Taiwan, in 1989.

From 1989 to 1998, he was an Assistant Researcher in the Chung-Sun Institute of Science and Technology (CSIST), Lung-Tan, Taiwan. In 1998, he joined the Institute of Computer Science and Information Engineering, National Central University. His current research interests include pattern recognition and image analysis.

Kuo-Chin Fan (S'88–M'88) was born in Hsinchu, Taiwan, on June 21, 1959. He received the B.S. degree in electrical engineering from National Tsing-Hua University, Hsinchu, Taiwan, in 1981. He received the M.S. and Ph.D. degrees from the University of Florida, in 1985 and 1989, respectively.

In 1983, he joined the Electronic Research and Service Organization (ERSO), Taiwan, as a Computer Engineer. From 1984 to 1989, he was a Research Assistant with the Center for Information Research, University of Florida. In 1989, he joined the Institute of Computer Science and Information Engineering, National Central University, Chung-Li, Taiwan, where he became a Professor in 1994. From 1994 to 1997, he was chairman of the department. Currently, he is the Director of the Computer Center. His current research interests include image analysis, optical character recognition, and document analysis.

Prof. Fan is a member of SPIE.